Extended gas in Seyfert 2 galaxies: implications for the nuclear source

Henrique A. Fraquelli,[1]★ T. Storchi-Bergmann[1] and N. A. Levenson[2]

[1]*Instituto de Física, UFRGS, 91501-970 Porto Alegre, RS, Brazil*
[2]*Department of Physics and Astronomy, Johns Hopkins University, Baltimore, MD 21218, USA*

ABSTRACT

We use long-slit spectroscopic optical data to derive the properties of the extended emitting gas and the nuclear luminosity of a sample of 18 Seyfert 2 galaxies. From the emission-line luminosities and ratios we derive the density, reddening and mass of the ionized gas as a function of distance up to 2–4 kpc from the nucleus. Taking into account the geometric dilution of the nuclear radiation, we derive the radial distribution of covering factors and the minimum rate of ionizing photons emitted by the nuclear source. This number is an order of magnitude larger than that obtained from the rate of ionizing photons 'intercepted' by the gas and measured from the Hα luminosity. A calibration is proposed to recover this number from the observed luminosity. The He II $\lambda 4686$/Hβ line ratio was used to calculate the slope of the ionizing spectral energy distribution (SED), which in combination with the number of ionizing photons allows the calculation of the hard X-ray luminosities. These luminosities are consistent with those derived from X-ray spectra in the eight cases for which such data are available and recover the intrinsic X-ray emission in Compton-thick cases. Our method can thus provide reliable estimates of the X-ray fluxes in Seyfert 2 galaxies for the cases where it is not readily available. We also use the ionizing SED and luminosity to predict the infrared luminosity under the assumption that it is dominated by reprocessed radiation from a dusty torus, and find a good agreement with the observed *IRAS* luminosities.

Key words: galaxies: active – galaxies: ISM – galaxies: Seyfert – X-rays: galaxies.

1 INTRODUCTION

Ionized gas in Seyfert galaxies is observed extending from tens of parsecs up to several kiloparsecs from the nucleus. A number of studies have been published showing the spatial distribution of this gas in narrow-band images (Mulchaey, Wilson & Tsvetanov 1996a), which is usually elongated and in some cases presents a clear cone-shaped morphology (Storchi-Bergmann, Wilson & Baldwin 1992a; Wilson et al. 1993).

The extended ionized gas is usually identified with the narrow-line region (NLR) of active galactic nuclei (AGN). Unger et al. (1987) have proposed a new terminology, extended narrow-line region (ENLR), to identify the outer parts of the extended ionized gas. The 'classical' NLR would be the inner part, which shows kinematic signatures of interaction with a radio-emitting plasma or an accretion disc wind, usually indicating the presence of outflows (e.g. Crenshaw et al. 2000). Detailed studies of the NLR, available for a few Seyfert galaxies (e.g. Crenshaw et al. 2000; Crenshaw & Kraemer 2000; Ruiz et al. 2001) indicate typical extents of up to ∼300 pc from the nucleus. The ENLR would correspond to the ionized gas beyond the NLR, where the gas velocities seem to be con-

sistent with rotation within the galaxy (Peterson 1997). The ENLR emission could thus be attributed to interstellar gas at kiloparsec scales in the host galaxies ionized by the AGN nucleus, and photoionization by the nuclear source seems to be the main mechanism producing the observed emission (Morse, Raymond & Wilson 1996; Evans et al. 1999). This conclusion is supported by self-consistent models applied to the ENLR (e.g. Nazarova, O'Brien & Ward 1997; Fraquelli, Storchi-Bergmann & Binette 2000, hereafter FSBB).

Once we know which are the dominant physical processes at play in the ENLR, the extended ionized gas can provide a 'periscopic view' of the nuclear region in Seyfert 2 galaxies, in which the ionizing source is hidden from direct view. By measuring the emission-line fluxes and ratios, and under the assumption that the emission lines are mainly produced by photoionization, gas properties such as mass, density and reddening, can be readily obtained, and the luminosities and spectral energy distribution (SED) of the ionizing sources.

Most recent works on the ENLR of Seyfert galaxies are detailed studies of only one galaxy. In this paper, our goal is to analyse the data of a larger sample – 18 Seyfert 2 galaxies, in order to look for common properties of the ionized gas and nuclear sources in Seyfert 2 galaxies. We have thus collected optical emission-line fluxes from long-slit data of the above sample at a typical spatial

★E-mail: ico@if.ufrgs.br

sampling at the galaxy of 100–300 pc. In this paper particular emphasis is placed on the derivation of the SED and luminosity of the central source, derived using the spatial distribution of emission-line fluxes and ratios along the ENLR.

2 OBSERVATIONS AND THE SAMPLE

High signal-to-noise ratio long-slit spectra of 18 Seyfert 2 galaxies with extended high excitation emission were obtained using the Cassegrain Spectrograph at the Blanco 4-m telescope of the Cerro Tololo Inter-American Observatory (CTIO) on 1992 May, 1994 January and December. The seeing was ∼1 arcsec, the spectral resolution ∼6 Å and the spectral range of the observations was 3500–7200 Å. The slit width corresponded to 2 arcsec on the sky. The slit was oriented along the maximum extent of the high excitation gas observed in narrow-band images centred on [O III] λ5007 (Mulchaey et al. 1996a). The average scale is 240 pc arcsec^{-1}, ranging from 48 pc arcsec^{-1} (for NGC 1386) to 570 pc arcsec^{-1} (for CGCG 420-015). More detailed information concerning the long-slit spectroscopy can be found in Cid Fernandes, Storchi-Bergmann & Schmitt (1998), where measurements of the absorption-line features as a function of distance from the nucleus are presented.

The sample comprises approximately 40 per cent of the Seyfert 2 galaxies from the catalogue of Veron-Cetty & Veron (2000) with $z < 0.02$ and luminosity in the [O III] λ5007 emission line larger than 10^{40} erg s^{-1}, which could be observed from the southern hemisphere. In addition, it contains the galaxies CGCG 420-015 and MCG-05-27-13, which obey the [O III] luminosity criterion but are somewhat more distant, with $z = 0.029$ and 0.024, respectively. Six of these galaxies have ENLR images obtained using narrow-band filters published by Mulchaey et al. (1996a).

Relevant information on the sample and observations are presented in Table 1: Hubble types (NED), radial velocity (RC3), absolute magnitude, date of the observations, position angle of the slit, scale, inclination of the galaxy (LEDA) and foreground Milky Way reddening. In the first column we include a number that was used to identify the galaxies in figures in the next sections. An asterisk identifies the galaxies with ENLR images in Mulchaey et al. (1996a).

3 RESULTS

Spectra were extracted using a 2-arcsec window centred on the optical nucleus. Off-nucleus spectra were also extracted using 2-arcsec windows up to approximately 10 arcsec from the nucleus, and ranging, on average, from 3 to 6 arcsec further out. The windows sizes can be recovered from Figs 2–4 (below) using the scales given in Table 1, considering that there are no gaps between windows.

As the nuclear extractions include gas emission within a few hundred parsecs from the nucleus for our sample, it is dominated by the high surface brightness NLR emission. According to Unger et al. (1987) the 'edge' between the NLR and the ENLR is defined by a change in the kinematic properties of the gas such that in the ENLR the FWHM drops below 45 km s^{-1} and the velocity field is characteristic of normal galactic rotation. Our spectral resolution does not allow the derivation of the kinematic properties of the ionized gas, precluding a clear separation between the NLR and ENLR. Nevertheless, recent works (e.g. Crenshaw et al. 2000; Ruiz et al. 2001) suggest an extent for the NLR of ∼300 pc. Thus, for our sample, the NLR should be mostly contained in the nuclear extraction with the exception of the closest galaxies NGC 1386, 5643 and 6300 (Table 1), for which the NLR could extend to the next one or two windows – if the NLR size above can be considered characteristic of most Seyfert galaxies. Besides these caveats we decided to refer to the nuclear extraction as the NLR and the off-nucleus ones as the ENLR, considering that these definitions do not change the main results of the present work.

Sample spectra of both the nuclear and extranuclear regions are shown in Fig. 1. Line emission was detected up to 2–4 kpc from the nuclei. The fluxes of the emission lines were measured as a function of distance from the nuclei by fitting Gaussians to the line profiles. Uncertainties in the fluxes were mostly caused by uncertainties in the placement of the continuum and were thus estimated as the product of the full-width at half-maximum of the line (FWHM) by the root-mean square deviation of the local continuum fluxes.

The angular distances were transformed to linear distances at the galaxies and corrected for inclination using the information listed in Table 1. Line luminosities were calculated adopting $H_0 = 75$ km s^{-1} Mpc^{-1}.

Table 1. Sample properties.

| Id	Galaxy	Morph.	v (km s^{-1})	Distance (Mpc)	M_B (mag)	Date	PA (deg)	Scale (pc arcsec^{-1})	i (deg)	$E(B-V)_G$ (mag)
1	ESO 417-G6*	(R)SA0/a	4792	63.89	−19.78	6/7 Jan 94	155	310	30.7	0.02
2	Fairall 316*	S0	4772	63.63	−19.94	6/7 Jan 94	100	308	44.4	0.19
3	CGCG 420-015*	Sa	8811	115.4	−20.69	6/7 Jan 94	40	570	12.5	0.07
4	IC 1816	(R'L)SA:(s:)a	5086	67.81	−20.61	6/7 Jan 94	90	328	33.1	0.03
5	IRAS 11215−2806	S0	4047	53.96	−20.97	5/6 Jan 94	145	262		0.09
6	MCG-05-27-13	SB(r)a	7263	277.8	−22.79	6/7 Jan 94	0	470	45.1	0.06
7	Mrk 1210	Sa	3910	52.13	−19.38	5/6 Jan 94	163	253	5.80	0.02
8	Mrk 607*	Sa:sp	2716	36.21	−19.68	6/7 Jan 94	135	176	80.9	0.02
9	NGC 1358*	SAB(r)0/a	3980	53.07	−20.60	6/7 Jan 94	145	257	53.6	0.03
10	NGC 1386	SB(s)0$^+$	741	9.88	−17.94	6/7 Jan 94	169	48	90.0	0.01
11	NGC 3081	SAB(r)0/a	2164	28.85	−19.69	28/29 May 92	73	140	51.7	0.03
12	NGC 5135	SB(1)ab	3959	52.79	−20.99	29/30 May 92	30	256	45.2	0.06
13	NGC 5643	SAB(rs)c	1066	14.21	−20.75	28/29 May 92	90	69	30.6	0.13
14	NGC 6300	SB(rs)b	997	14.80	−20.29	28/29 May 92	124	63	54.6	0.12
15	NGC 6890	SB(r)ab	2459	40.71	−19.74	29/30 May 92	153	159	40.1	0.01
16	NGC 7130	Sa pec	4850	64.67	−21.20	20/30 May 92	143	314	33.2	0.03
17	NGC 7582	SB(s)ab	1551	20.68	−20.27	6/7 Jan 94	67	100	70.1	0.01
18	Mrk 348*	SA(s)0/a	4669	62.25	−20.36	6/7 Dec 94	170	302	46.5	0.06
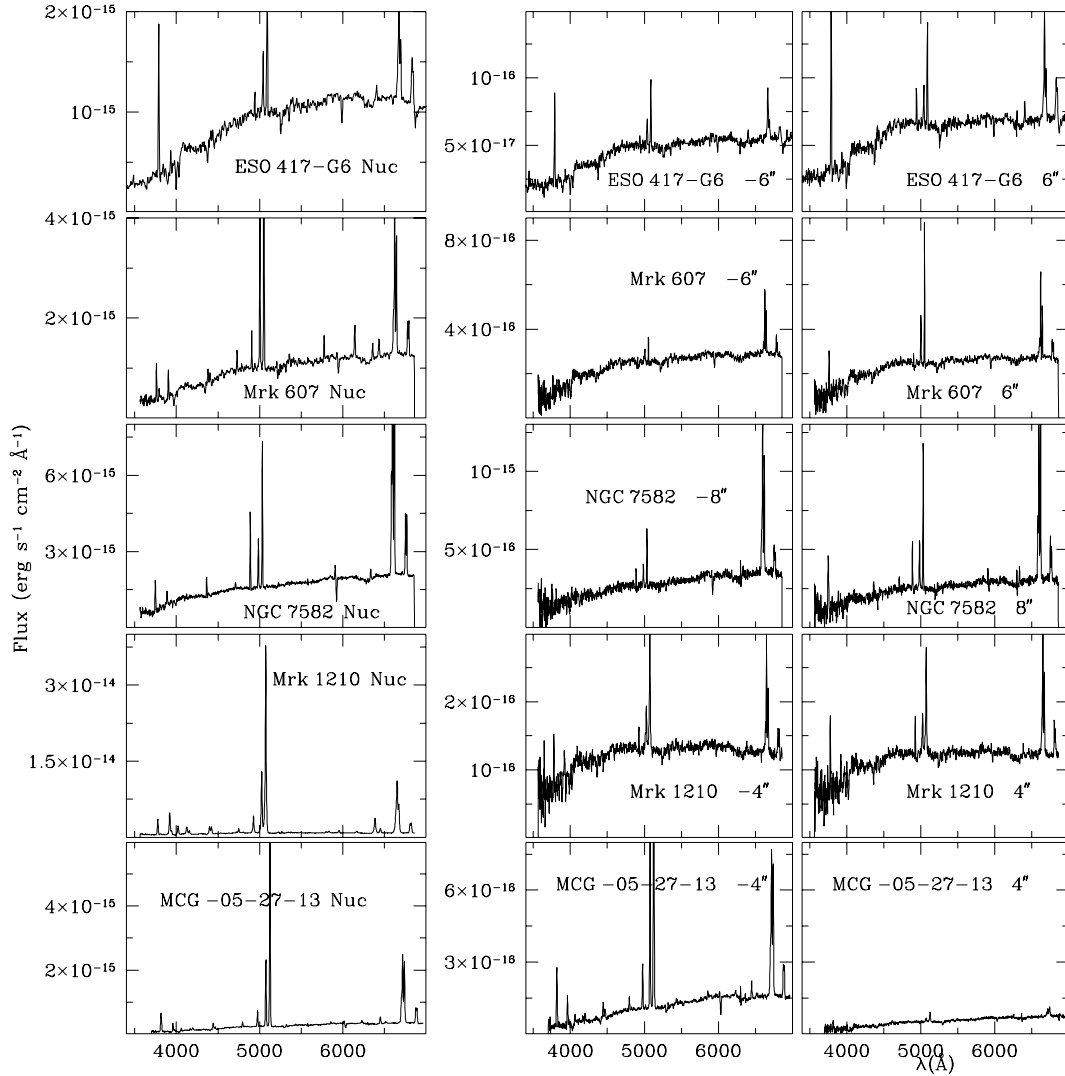
Figure 1. Sample of some spectra used in this work.

3.1 Reddening distributions

We have used the Balmer decrement $H\alpha/H\beta$ to derive the distribution of reddening as a function of distance from the nucleus in 14 of the sample galaxies. We corrected for foreground Milky Way extinction and assumed the intrinsic ratio of $H\alpha/H\beta = 3.1$ (Osterbrock 1989). The resulting $E(B - V)$ ranges from 0.3 to 1.2 along the ENLR, with typical nuclear values of $E(B - V) \simeq 0.6$, as shown in Fig. 2. In the cases where we could not measure the $H\beta$ emission line, because it was superposed on the $H\beta$ absorption line from the stellar component, we interpolated the reddening determined for the neighbouring locations. Although this interpolation is uncertain we believe it is a better representation of the actual $E(B - V)$ than using no reddening at all. For NGC 6300, IRAS 11215−2806 and Fairall 316, $H\beta$ is too weak to be measured in most locations. For these cases we have obtained only lower limits for $E(B - V)$, which have been used to correct the emission-line fluxes.

In eight galaxies we deduced lower reddening in the nuclear region compared with the neighbouring locations further out. This is contrary to what might be expected, considering the dusty environment of Seyfert 2 nuclei (Antonucci 1993; Martini & Pogge 1999).

This type of variation of $E(B - V)$ with radial distance had been previously found by Veilleux et al. (1995) for one Seyfert 2 galaxy and two LINERs out of a sample of 19 AGNs. They considered two possibilities. The first is that some Seyfert galaxies have a smaller amount of dust in the nucleus owing to dust destruction/expulsion by the ionizing radiation field generated in the AGN and/or by shocks. The second possibility is complex optical depth effects such that the inner regions could be optically thick to the optical emission. We attribute the higher incidence of this kind of behaviour in our work as compared with that of Veilleux et al. (1995) to the better spatial resolution of our data, as the data-taking procedure of Veilleux et al. was not optimized to obtain spatial information on the objects of their sample.

In order to investigate whether the reddening behaviour could be a result of the fact that we did not take into account the underlying absorption owing to the contribution of the stellar population (which can be large in the case of $H\beta$) we have attempted to correct our data for this effect. First, we adopted a constant value of 2 Å for the equivalent width of both $H\beta$ and $H\alpha$ absorptions, a procedure frequently used in previous works. The result was many negative values for $E(B - V)$, indicating that $H\beta$ was overestimated. We have then used the spectrum of the nucleus of the normal galaxy
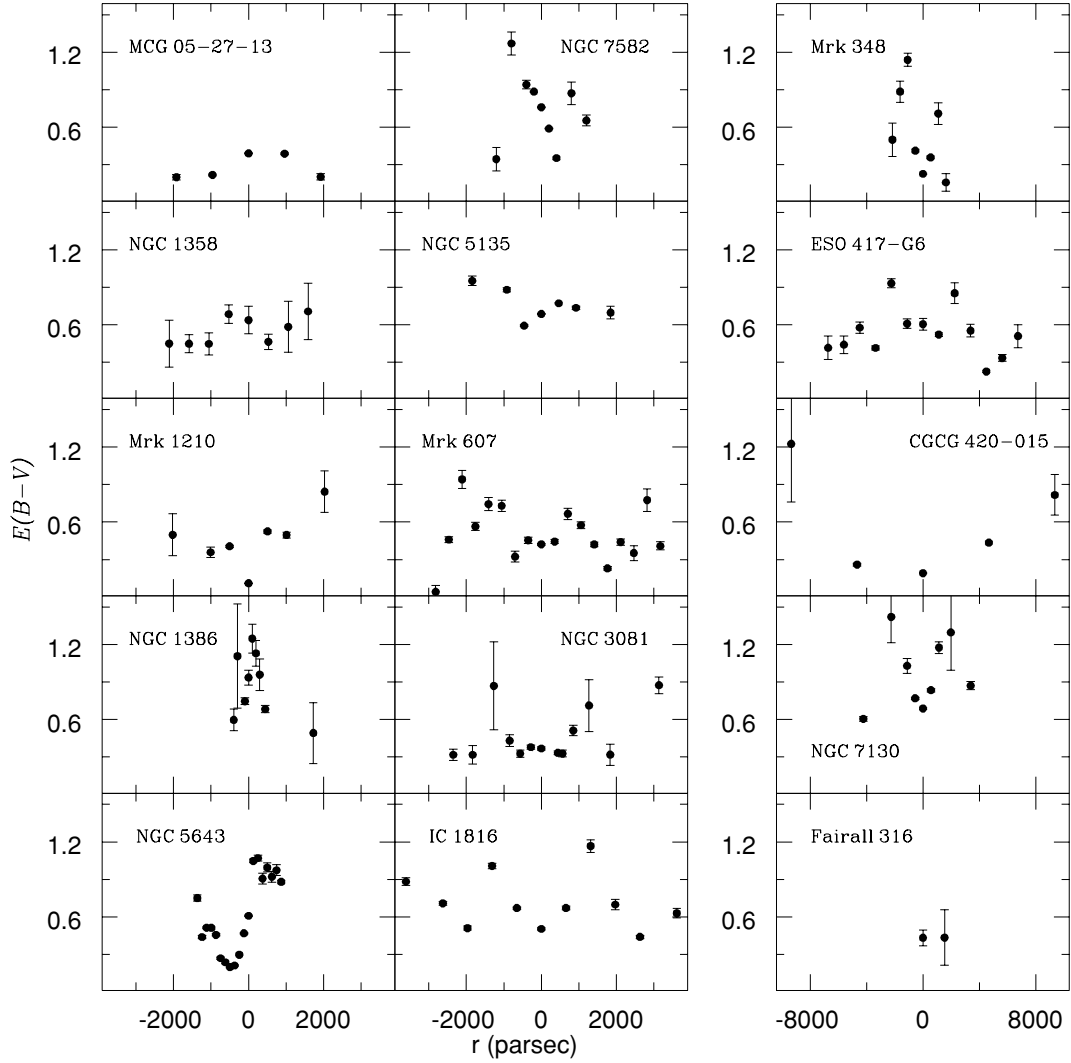
Figure 2. $E(B - V)$ as a function of the distance from the nucleus for 15 Seyfert 2 galaxies.

NGC 6684 to correct the spectra for the underlying absorption. This method did not give negative values for $E(B - V)$ and made the distribution flatter only for two of the eight galaxies for which we had found smaller $E(B - V)$ values at the nucleus. We thus conclude that the effect is real. The reddening was used to correct all emission-line fluxes, adopting the Seaton (1979) reddening law.

3.2 Electron density distributions

The electron density distribution, derived from the emission-line ratio [S II] $\lambda6731$/[S II] $\lambda6717$ (Osterbrock 1989) is shown in Fig. 3 for 14 galaxies of our sample. For CGCG 420-015 the [S II] emission lines could not to be measured. The gas at the nucleus has densities in the range $300 \leqslant n_e \leqslant 1000\ cm^{-3}$, which decrease outwards down to the low-density limit, assumed to be 50 cm^{-3}, at the most distant locations (>2 kpc) from the nucleus. The nuclear regions have an average density of $440 \pm 200\ cm^{-3}$, similar to that obtained by Veilleux et al. (1995; $\sim430\ cm^{-3}$).

3.3 Luminosity distributions

We have calculated the luminosities in the emission lines [O III] and Hα as well as in the continuum underlying [O III] along the

ENLR from the emission-line fluxes and distances listed in Table 1. In order to allow a comparison among all galaxies of the sample, we have divided the integrated luminosity in each window by the corresponding area in square parsecs at the galaxy. These 'surface luminosity distributions' L^{area} – corrected for the galactic and internal reddening, obtained in Section 3.1 – are shown in Fig. 4.

The [O III] surface luminosity distributions are, on average, more centrally peaked than those of [O II] $\lambda3727$ and Hα. This means that the excitation is higher close to the nucleus, with the ionization parameter seen by the gas decreasing with radius. The possible presence of H II regions in the disc of the host galaxies will also contribute to this behaviour. Fig. 5 shows a comparison between the nuclear surface luminosities in [O III] and Hα, showing that most of the galaxies of our sample present a nuclear ratio [O III]/Hα roughly constant with luminosity, with a ratio of approximately 3–4.

We fitted a power-law function $F = F_0 r^\delta$ to the surface luminosity distributions above, and to the density of the ionized gas obtained from the [S II] ratio. The fitting parameters are shown in Table 2 where L_0 corresponds to the surface luminosities at 100 pc from the nucleus. The [O III] luminosity falls faster with the radius than the Hα luminosity, with an average index for the power law of $\delta = -3.2 \pm 0.8$, excluding from the average the galaxies with poor fits
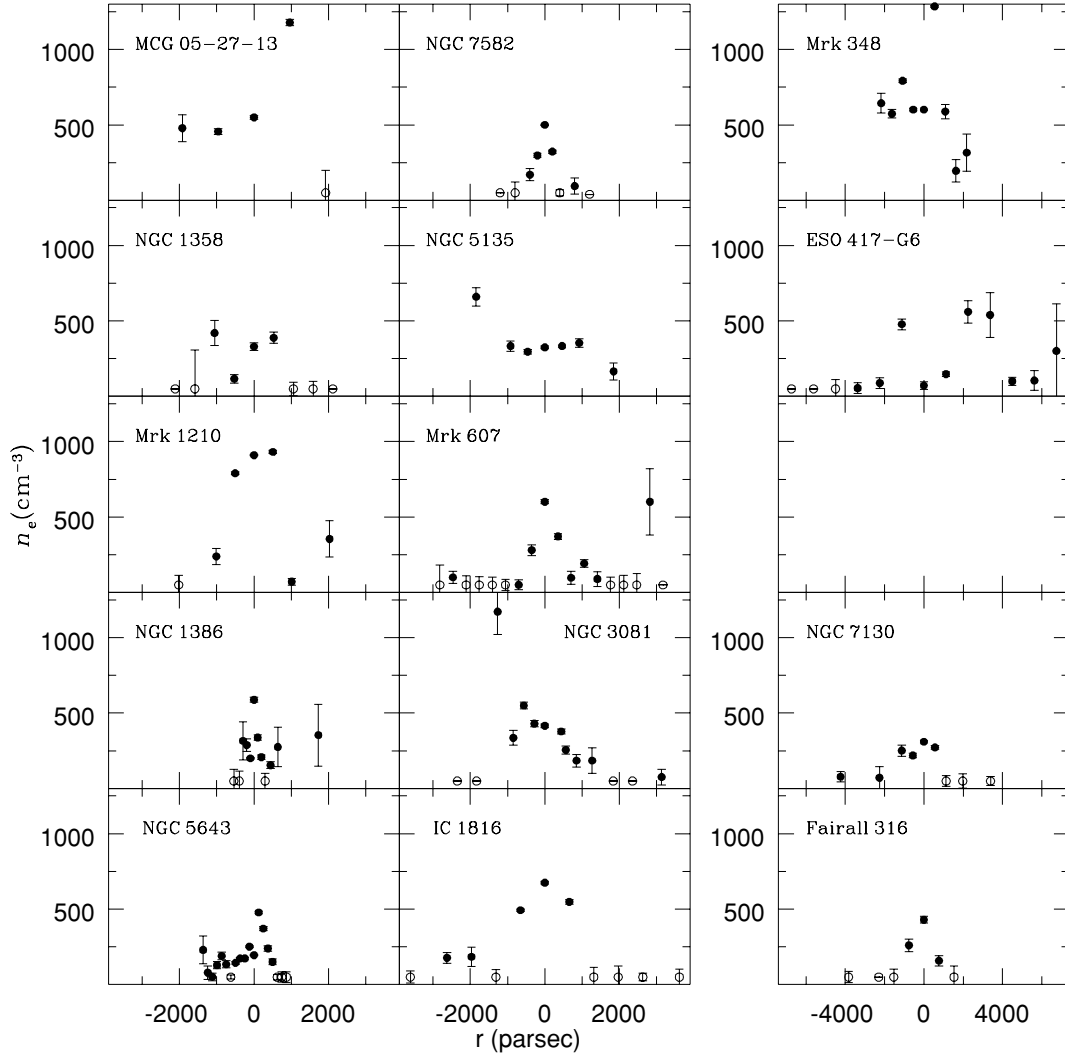
Figure 3. Electron density obtained from [S II] ratio as a function of the distance from the nucleus. Open symbols are locations where n_e is the in low-density limit (assumed $\leqslant 50$ cm^{-3}).

(identified by colons in the fitting parameters) due in most cases to an insufficient number of data points. For the Hα luminosity the average index is -2.4 ± 0.7. The gas density has an average index of $\delta = -0.9 \pm 0.3$.

In order to assess the meaning of the above distributions, we use Osterbrock (1989) to express the Hβ luminosity of a nebula with a filling factor ϵ and ionized gas density n (assuming that $n_e = n_{ions} = n$) as

$$L_{H\beta} = \int \alpha_{H\beta}^{eff} h\nu_{H\beta} n^2 \epsilon \, dV, \tag{1}$$

where dV is the element of volume and $\alpha_{H\beta}^{eff}$ is the effective Hβ recombination coefficient. In the locations where $L_{H\beta}$ could not be measured its value was obtained from the corrected Hα luminosity.

If we assume that ϵ and n are constant within each window, we obtain

$$L_{H\beta} = \alpha_{H\beta}^{eff} h\nu_{H\beta} n^2 \epsilon V_{tot} = \alpha_{H\beta}^{eff} h\nu_{H\beta} n^2 V_{gas}, \tag{2}$$

where V_{tot} is the total volume corresponding to each window, and $V_{gas} = \epsilon V_{tot}$ is the effective volume occupied by the ionized gas.

Using the average indices for $L_{H\alpha}$ and n distributions we obtain, from equation (2) above, $V_{gas} \propto r^{-0.6}$. However, considering the

uncertainties, this result is also consistent with $V_{gas} \sim$ constant along the ENLR.

### 3.4 Surface mass distribution of the ionized gas

The ionized gas mass (integrated in the extraction windows) was obtained from the Hβ luminosity and the gas density (Peterson 1997) using the expression below:

$$M_{H^+} = 7 \times 10^8 \frac{L_{H\beta}^{41}}{n_e} \, M_\odot, \tag{3}$$

where $L_{H\beta}^{41}$ is the Hβ luminosity in units of 10^{41} erg s^{-1}, n_e is the electron density in units of cm^{-3} and M_{H^+} is the ionized gas mass (in solar units) within the extracted window. We point out that M_{H^+} is a lower limit for the windows where the density is lower than the adopted 50 cm^{-3} (open symbols in Fig. 3). The total ionized gas and the nuclear (NLR) gas masses are listed in Table 3. The total mass, including the contributions of nucleus (NLR) and ENLR range from $\approx 10^5$ to 10^7 M$_\odot$ Inspecting the narrow-band images of the galaxies of our sample available in Mulchaey et al. (1996a) we estimate that, on average, our slit covers approximately one-third
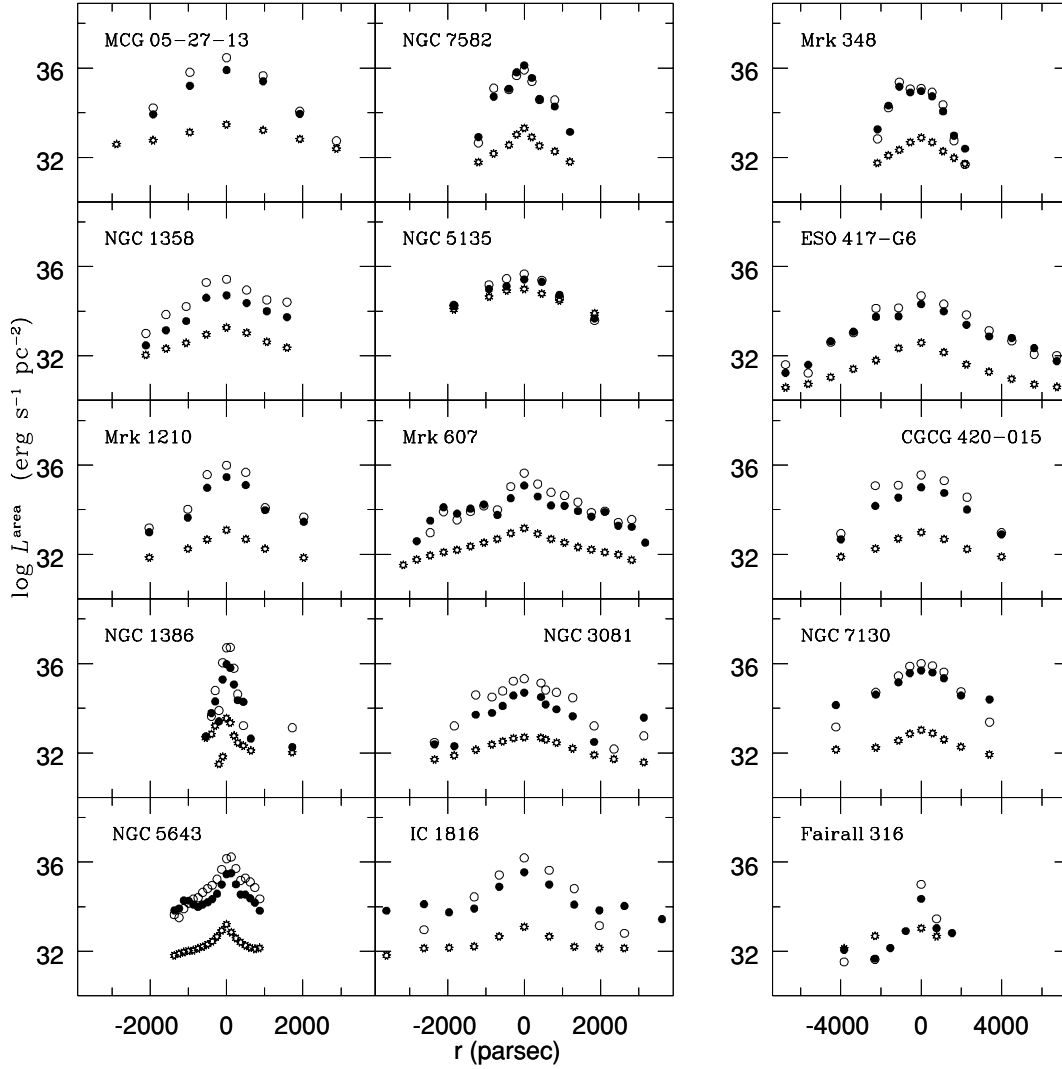
Figure 4. Surface luminosity distribution in Hα (filled symbols), [O III] λ5007 (open symbols) and 5000-Å continuum (star symbols). Error bars are smaller than the symbols sizes.
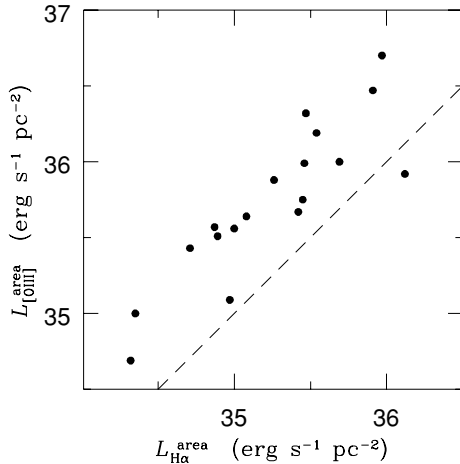
Figure 5. Comparison between Hα and [O III] surface nuclear (NLR) luminosities. The dashed line shows the loci of $L_{H\alpha}^{area} = L_{[O\,III]}^{area}$, for reference.

of the area occupied by the emitting gas in the images. Therefore, the total ionized gas mass could be as large as three times the value listed in (3).

In order to compare the ionized mass distribution of different galaxies, we have calculated an ionized gas mass per unit area, using the following expression:

$$M_{H^+}^{area} = 7 \times 10^8 \left(\frac{L_{H\beta}^{41}}{A_w} \right) n_e^{-1} \, M_\odot \, pc^{-2}, \tag{4}$$

where A_w is the area in square parsecs corresponding to the extraction window (in most cases 2×2 arcsec^2). Fig. 6 shows the above mass as a function of distance from the nucleus. In most cases the profiles show a peak on the nucleus, with values between 0.12 and $5.9 \, M_\odot \, pc^{-2}$ and an average of $1.8 \pm 1.7 \, M_\odot \, pc^{-2}$, decreasing outwards. In a few cases, the ENLR values are similar to those at the nucleus.

We have considered the effect of a larger density for the NLR than that derived from the [S II] ratio in the calculated gas masses. In the extreme case that all the gas has a density of $n_e = 10^4$ cm^{-3}, the NLR masses would decrease typically by one order of magnitude,

Table 2. Fitting parameters. L_0 corresponds to the surface luminosities 100 pc from the nucleus.[a]

Galaxy	log L_0 [O III]	$\delta_{[O\,III]}$	log L_0 Hα	$\delta_{H\alpha}$	log L_0 Cont-5000 Å	$\delta_{Cont-5000\,\text{Å}}$	log n_0 [S II]	δ_{n_e}
ESO 417-G6	38.30	−3.5	37.32	−2.9	34.59	−2.2	4.1	−0.7
Fairall 316	35.91	−2.9	34.38	−1.6	35.30	−2.9	5.0	−1.0
CGCG 420-015	39.71	−4.0	38.33	−3.4	34.26	−1.5		
IC 1816	39.13	−4.3	36.03	−1.6	33.67	−1.2	5.6	−1.1
IRAS 11215−2806	41.39	−8.5			33.93	−1.4		
MCG -05-27-13	40.94	−5.3	39.78	−4.6	34.42	−1.3	7.3	−1.6
Mrk 1210	38.02	−3.7	37.07	−3.0	33.63	−1.4	6.4	−1.3
Mrk 607	36.31	−2.1	35.54	−1.6	33.83	−1.4	4.4	−0.8
NGC 1358	37.73	−3.4	36.58	−2.8	34.29	−1.7	5.4	−1.2
NGC 1386	35.92	−2.9	35.39	−2.8	33.25	−1.4	4.3	−0.9
NGC 3081	37.12	−3.0	36.15	−2.6	33.40	−1.2	5.6	−1.1
NGC 5135	37.16	−2.5	36.67	−2.1	35.85	−1.4	3.6	−0.4
NGC 5643	36.33	−2.2	35.26	−1.3	32.99	−1.0	4.2	−0.8
NGC 6300	35.79	−2.8	35.09	−3.3	33.21	−0.2		
NGC 6890	37.03	−3.1	36.11	−2.7	33.00	−0.8	4.0	−0.6
NGC 7130	38.50	−3.1	36.89	−1.7	33.61	−1.0	4.3	−0.7
NGC 7582	36.42	−2.5	36.69	−3.0	33.41	−1.4	4.8	−1.0
Mrk 348	38.65	−4.4	37.46	−3.2	33.84	−1.5		

[a] In units of erg s^{-1} pc^{-2}.

Table 3. Ionized gas mass.

Id	Galaxy	Total mass ($10^3\,M_\odot$)	NLR mass ($10^3\,M_\odot$)
1	ESO 417-G6	1421	830
2	Fairall 316	97	55
3	CGCG 420-015		
4	IC 1816	2030	497
5	IRAS 11215−2806	519	396
6	MCG -05-27-13	4637	3047
7	Mrk 1210	467	183
8	Mrk 607	639	56
9	NGC 1358	546	93
10	NGC 1386	124	33
11	NGC 3081	247	27
12	NGC 5135	1477	478
13	NGC 5643	239	62
14	NGC 6300	77	15
15	NGC 6890	199	43
16	NGC 7130	13422	1400
17	NGC 7582	1044	237
18	Mrk 348	390	103

and become comparable to the values of the windows corresponding to the extranuclear regions.

4 THE IONIZING LUMINOSITY

The rate of ionizing photons, Q, intercepted by the gas in each window is related to its Hβ luminosity through the expression (Osterbrock 1989):

$$Q = \frac{L_{H\beta}\alpha_B}{\alpha_{H\beta}^{eff} h\nu_{H\beta}}, \tag{5}$$

where α_B is the case B recombination coefficient and $\alpha_{H\beta}^{eff}$ is the effective Hβ recombination coefficient. Table 4 shows the nuclear value, Q_{nuc} (which we consider as corresponding to the unre-

solved NLR), and the sum of the values from all windows, Q_{sum} (NLR+ENLR).

Q_{sum} is the ionizing photon rate one obtains from single-aperture studies (e.g. Kinney et al. 1991), which do not take into account either the dilution of the nuclear radiation with distance from the nucleus or the fact that, for each window, the area facing the source is not totally covered by gas. Q_{sum} thus underestimates the rate of ionizing photons *emitted* by the source, which we will call Q_{AGN}.

In order to obtain Q_{AGN}, it is necessary to take into account the two aspects mentioned above. For a central source emitting Q_{AGN}, the photon rate that crosses the unit area at a distance r from the source is $Q_{AGN}/4\pi r^2$. The photon rate intercepted by the gas in each window is proportional to the fraction of its area facing the source that contains gas, which we will call the covering factor of the window $C(r)$ (which is different from the usual definition of the covering factor, the ratio between the solid angle of a gas cloud and 4π).

The ionizing photon rate per unit area intercepted by the gas in each window is

$$Q(r) = C(r)\frac{Q_{AGN}}{4\pi r^2}. \tag{6}$$

Q_{AGN} can thus be obtained for each window

$$Q_{AGN} = \frac{Q(r)}{C(r)}4\pi r^2 = \frac{4\pi r^2 L_{H\beta}^{sup}}{C(r)}\frac{\alpha_B}{\alpha_{H\beta}^{eff} h\nu_{H\beta}}, \tag{7}$$

where we have used equation (5) for $Q(r)$, replacing $L_{H\beta}$ by $L_{H\beta}^{sup} = L_{H\beta}/A_{section}$, where $A_{section}$ is the area facing the source. This expression considers both the geometric dilution of the nuclear power and the covering factor of the gas facing the source.

In order to calculate $L_{H\beta}^{sup}$, we have adopted two different geometries for each window: (i) a box geometry, where the depth along the line of sight is equal to the linear extent of the window in the plane of the sky; (ii) a conical geometry such that $A_{section} = 2\,lr\,\tan(\theta)$ (as used by FSBB), where l is the linear extent at the galaxy corresponding to 2 arcsec (slit width), r is the distance between the centre of the window and the source and θ is half the opening angle of the cone of ionizing radiation. We have used $\theta = 30°$ as
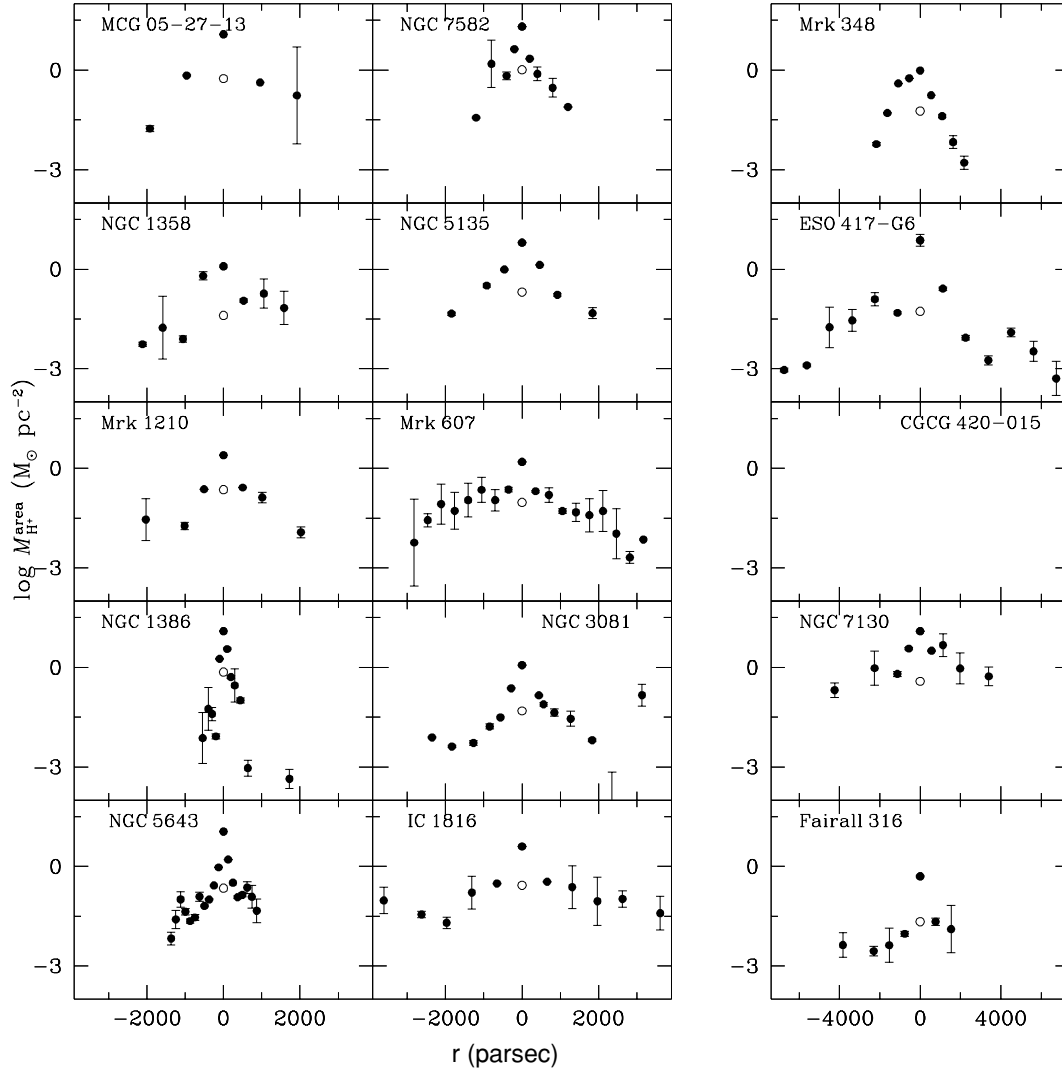
Figure 6. Ionized gas mass per unit area as a function of the distance from the nucleus. Open symbols show the value for the NLR if $N_e = 10^4$ cm^{-3} instead of that obtained from the [S II] ratio.

representative of the opening angle observed in ionization cones of Seyfert 2 galaxies (Mulchaey, Wilson & Tsvetanov 1996b).

In the case of the nuclear extraction (corresponding to the NLR in many cases) we have adopted an effective distance from the ionizing source of 0.5 arcsec, as the extraction window corresponds to 1 arcsec to each side of the nucleus. In the conical geometry we have used $A_{\text{section}} = \pi r^2 \tan^2(\theta)$ for the NLR, and $L_{\text{H}\beta}^{\text{sup}}$ was divided by 2 assuming that we are seeing both sides of the ionization cone.

We have first calculated lower limits for Q_{AGN} using equation (7), for each window with $C(r) = 1$ (which we will call Q'_{AGN}). These values are shown in Fig. 7 for both the box geometry (open circles) and the conical geometry (filled circles). For most galaxies these minimum values derived for all windows are remarkably similar along the ENLR. These similar values suggest that each location absorbs the same number of ionizing photons per unit area.

If the gas clouds are ionization-bounded, the assumption of $C(r) = 1$ within each window is not correct, because it means that the gas should absorb all the ionizing photons and none would reach the subsequent window. However, this cannot be correct because the ionized gas extends to large distances from the nucleus, being present in many subsequent windows – implying that the covering

factor must be smaller than unity. Indeed, in FSBB it was found that $C(r) \sim 0.1$ for the ENLR. Thus, in order to calculate the correct value for Q_{AGN} we need to know $C(r)$.

4.1 Covering factor

The covering factor $C(r)$ of each window is the fraction of the area facing the ionizing source covered by the gas, and can be calculated as

$$C(r) = \frac{A_{\text{gas}}(r)}{A_{\text{section}}(r)}, \tag{8}$$

where A_{gas} is the area effectively occupied by the gas and A_{section} is the area of the geometrical section of the window intercepting the ionizing beam. A_{section} was calculated using the conical geometry (as described in the previous section), and A_{gas} as

$$A_{\text{gas}} = \frac{M_{\text{H}^+}\eta}{N_{\text{H}^+}}, \tag{9}$$

where M_{H^+} is the ionized gas mass in each window (from equation 3) in solar mass units, η is the number of H$^+$ ions in one solar mass and N_{H^+} is the gas column density.

Table 4. Ionizing photons rates Q, covering factor for the NLR, H^+ column density and spectral indices.

Galaxy	log $Q_{\rm nuc}$	log $Q_{\rm sum}$	log $Q_{\rm ENLR}$ $\alpha = 1.5$	log $Q_{\rm AGN}$ $\alpha = 1.5$	log $Q_{\rm AGN}$ $\alpha_{\rm He\,II}$	$C_{\rm NLR}$ $\alpha_{\rm He\,II}$	log $\overline{N}_{\rm H^+}$ (cm^{-2})	$\alpha_{\rm He\,II} \pm \sigma_\alpha$
ESO 417-G6	52.25	52.63	53.38	53.62	53.68	0.48	20.8	1.76 ± 0.46
Fairall 316	51.85	51.90	51.89	52.68	52.70	0.83	20.0	–
CGCG 420-015	52.94	53.28	53.73^a	53.73^a	–	–	–	1.50 ± 0.03
IC 1816	53.00	53.24	53.91	54.24	54.32	0.54	21.1	1.59 ± 0.16
IRAS 11215−2806	52.74	52.83	53.09	53.76	53.54	0.74	21.3	0.94 ± 0.00
MCG -05-27-13	53.70	53.89	54.28	54.83	54.89	0.73	21.5	1.46 ± 0.27
Mrk 1210	52.70	52.97	53.52	53.87	53.95	0.57	20.9	1.59 ± 0.07
Mrk 607	52.00	52.42	53.69	53.78	53.46	0.19	20.8	1.02 ± 0.32
NGC 1358	51.96	52.38	53.08	53.29	53.27	0.38	20.6	–
NGC 1386	51.76	52.09	53.02	53.24	52.83	0.34	21.7	0.82 ± 0.02
NGC 3081	51.52	52.18	53.03	53.14	52.85	0.10	20.3	0.93 ± 0.01
NGC 5135	52.67	53.16	54.08	54.25	54.26	0.33	21.4	1.51 ± 0.21
NGC 5643	51.56	52.14	53.27	53.38	53.19	0.23	21.7	1.03 ± 0.17
NGC 6300	51.28	51.57	52.08	52.42	52.42	0.53	21.2	–
NGC 6890	51.55	52.08	52.91	53.09	52.84	0.32	20.8	0.96 ± 0.10
NGC 7130	53.11	53.72	54.87	54.98	55.07	0.23	21.8	1.66 ± 0.13
NGC 7582	52.55	52.87	53.85	54.22	54.21	0.42	21.9	1.73 ± 0.30
Mrk 348	52.27	52.92	54.17	54.17	54.17	0.37	21.6	1.62 ± 0.15

^{a}Maximum log $Q_{\rm AGN}$ obtained along the ENLR assuming $C(r) = 1$.

The value of $N_{\rm H^+}$ was obtained using the photoionization code MAPPINGSIC (Binette, Wilson & Storchi-Bergmann 1996), for the gas density obtained in Section 3.2 and assuming a spectral energy distribution $L_\nu \propto \nu^{-\alpha}$, with $\alpha = 1.5$, for photons with $h\nu \geqslant 13.6$ eV and solar metallicity. For a cloud at a distance r from a source that radiates $Q_{\rm AGN}'$ ionizing photons per unit time, the code gives the column $N_{\rm H^+}$ for which the ionization fraction H^+/H reaches values smaller than 1 per cent of the maximum.

The normalization value of the central source luminosity was initially adopted to give the maximum $Q_{\rm AGN}'$ along the ENLR under the hypothesis that $C(r) = 1$. This rate of ionizing photons was then diluted by the distance to each location along the ENLR to obtain $N_{\rm H^+}$ in the hypothesis that the clouds are ionization-bounded.

For the models to be consistent, the sum of covering factors $\sum C_{\rm ENLR}(r)$ along the ENLR cannot exceed unity (for each side of the nucleus). This constraint also ensures that the central source generates the necessary number of photons to ionize the entire ENLR. Only for Mrk 607, MCG 05-27-13, IRAS 11215−2806, Fairall 316, ESO 417-G6 and Mrk 348 did we obtain $\sum C_{\rm ENLR}(r) \leqslant 1$. In the remaining cases, we originally found it to be larger than unity. We have thus increased the luminosity of the central source until $\sum C_{\rm ENLR}(r) \leqslant 1$. The resulting number of ionizing photons per unit time $Q_{\rm ENLR}$ obtained as the sum of the contributions from all windows is also shown in Table 4.

We have next included the contribution of the nuclear extraction (NLR) in the calculations with the constraint that $\sum C_{\rm ENLR} + C_{\rm NLR} \leqslant 1$. Fig. 8 shows the $C_{\rm NLR}$ value and the $C_{\rm ENLR}$ distributions along the ENLR. The values for the NLR range from 0.2 to 0.8, while for the ENLR the average value is $C(r) = 0.1$ (as in FSBB).

4.2 Nuclear ionizing photon rate $Q_{\rm AGN}$

Adding the contributions from both the NLR and the ENLR we have derived the total number of ionizing photons $Q_{\rm AGN}$, shown in Table 4 and as dashed line in Fig. 7. This number ranges from $10^{52.5}$ to 10^{55} photon s^{-1} (with an average value of $Q = 10^{54.17 \pm 1.7}$ photon s^{-1}). We also list in Table 4 the total ionized gas column, calculated as

$$\overline{N}_{\rm H^+} = \frac{\sum C(r) N_{\rm H^+}}{\sum C(r)}. \tag{10}$$

The actual source could be even more luminous if some photons escape or are not detected. We thus regard all values of Q in Table 4 as minimum values. A comparison between $Q_{\rm ENLR}$ and $Q_{\rm AGN}$ shows that, on average, two-thirds of the ionizing photons are absorbed in the ENLR and the remaining one-third in the NLR.

The $Q_{\rm AGN}$ value quoted in Table 4 can be compared with $Q_{\rm sum}$. The latter, which has been frequently used in previous works to estimate the nuclear source luminosity, underestimates $Q_{\rm AGN}$ by approximately one order of magnitude. This is illustrated in Fig. 9, which shows the relation between the total $H\alpha$ luminosity (NLR+ENLR) and both $Q_{\rm sum}$ and $Q_{\rm AGN}$. A linear regression to the relation between $Q_{\rm AGN}$ and the total $H\alpha$ luminosity gives

$$\log Q_{\rm AGN} = 7.55 + 1.128 \log L_{\rm H\alpha}^{\rm tot} \tag{11}$$

for $L_{\rm H\alpha}^{\rm tot}$ in erg s^{-1}. This relation can be used to estimate the number of ionizing photons per unit time of a nuclear source once the $H\alpha$ luminosity is known.

4.3 Effects of a different SED on $Q_{\rm AGN}$

Previous studies, for example Cid Fernandes et al. (1998) and Storchi-Bergmann et al. (2000), identified circumnuclear starbursts in four of our sample galaxies: NGC 5135, 7130, 7582 and Mrk 1210. In the cases of NGC 5135 and 7130 the bolometric luminosity of the starburst seems to be comparable to that of the AGN (González-Delgado, Heckman & Leitherer 2001). In order to investigate the implication of the above result we have calculated the bolometric luminosities of a starburst with an SED given by Schmitt et al. (1997) and that of an AGN with an SED given by Elvis et al. (1994) for radio-quiet quasars. For equal values of bolometric luminosities we obtained that ~35 per cent of the number of ionizing photons per second is contributed by the starburst. Thus, the values of $Q_{\rm AGN}$ could be down to ~65 per cent of the values listed in Table 4 for NGC 5135 and 7130. The same should apply to NGC 7582 and Mrk 1210.
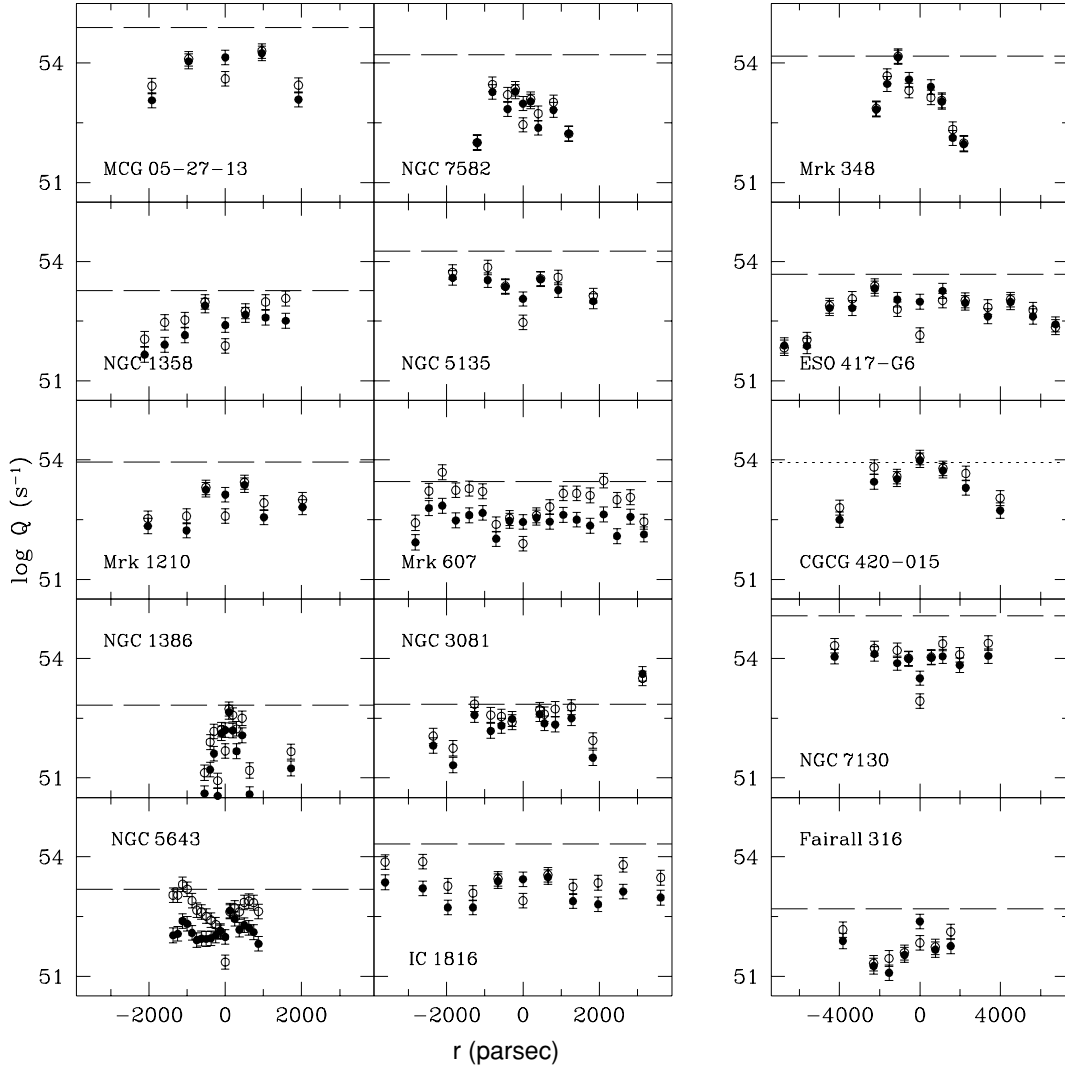
Figure 7. Minimum rate of ionizing photons $Q_{AGN}{}'$ radiated by the AGN calculated from the Hβ luminosities of each window for $C(r) = 1$ and both the conical geometry (filled symbols) and box geometry (open symbols). The long dashed line represents the value of the total rate of ionizing photons Q_{AGN} calculated in Section 4.1.

We have also investigated the effects of a higher gas density for the NLR than that obtained from the [S II] ratio. For $n_e = 10^4$ cm^{-3}, the resulting C_{NLR} are ≈ 10 per cent smaller and the effect in log Q_{AGN} is to decrease its value by at most 0.2 dex. In addition, we have tested other values of α besides 1.5 and verified that C does not vary much: the value of C for $\alpha = 1.5$ is ≈ 40 per cent larger than that for $\alpha = 1.0$ and ≈ 20 per cent smaller than that for $\alpha = 2.0$.

4.4 He$^+$ ionizing photons

The luminosity in the He II $\lambda 4686$ emission line can be used to calculate the rate at which ionizing photons with $h\nu \geqslant 54.4$ eV reach each window. Similarly to equation (5), for He II $\lambda 4686$ we have (Osterbrock 1989)

$$Q(\text{He}^+) = \frac{L_{\text{He}^+}\alpha_B^{\text{He}^+}}{\alpha_{\text{He}^+}^{\text{eff}} h\nu_{\text{He}^+}}, \tag{12}$$

where $\alpha_B^{\text{He}^+}$ is the He II recombination coefficient in case B and $\alpha_{\text{He}^+}^{\text{eff}}$ is the effective He II $\lambda 4686$ recombination coefficient.

For the locations in which we measure both He II and Hβ emission we can derive the slope $\alpha_{\text{He II}}$ of the ionizing continuum between 13.6 and 54.4 eV, under the assumption that $L_\nu \propto \nu^{-\alpha_{\text{He II}}}$. The slope is given by

$$\alpha_{\text{He II}} = \frac{\log\left[Q(\text{H}^+)/Q(\text{He}^+)\right]}{\log 4}. \tag{13}$$

The values derived for $\alpha_{\text{He II}}$ using the expression above are listed in the final column of Table 4. The average for the whole sample is $\alpha_{\text{He II}} = 1.3 \pm 0.3$. However, instead of being evenly spread around the average, the $\alpha_{\text{He II}}$ values seem to cluster around two values: $\alpha_{\text{He II}} = 1.6 \pm 0.1$ (eight cases) with values varying from 1.46 to 1.76 and $\alpha_{\text{He II}} = 1.0 \pm 0.1$ (six cases) with values varying from 0.82 to 1.03. We note that four of the eight galaxies with softer ionizing spectra are those with circumnuclear starbursts (see the previous section), in which part of the ionization is caused by young stars. Using the starburst models of Leitherer & Heckman (1995), we verified that the predicted $\alpha_{\text{He II}}$ using equation (13) for a pure starburst is ≈ 1.66, consistent with an important contribution of the starburst in the above four cases.
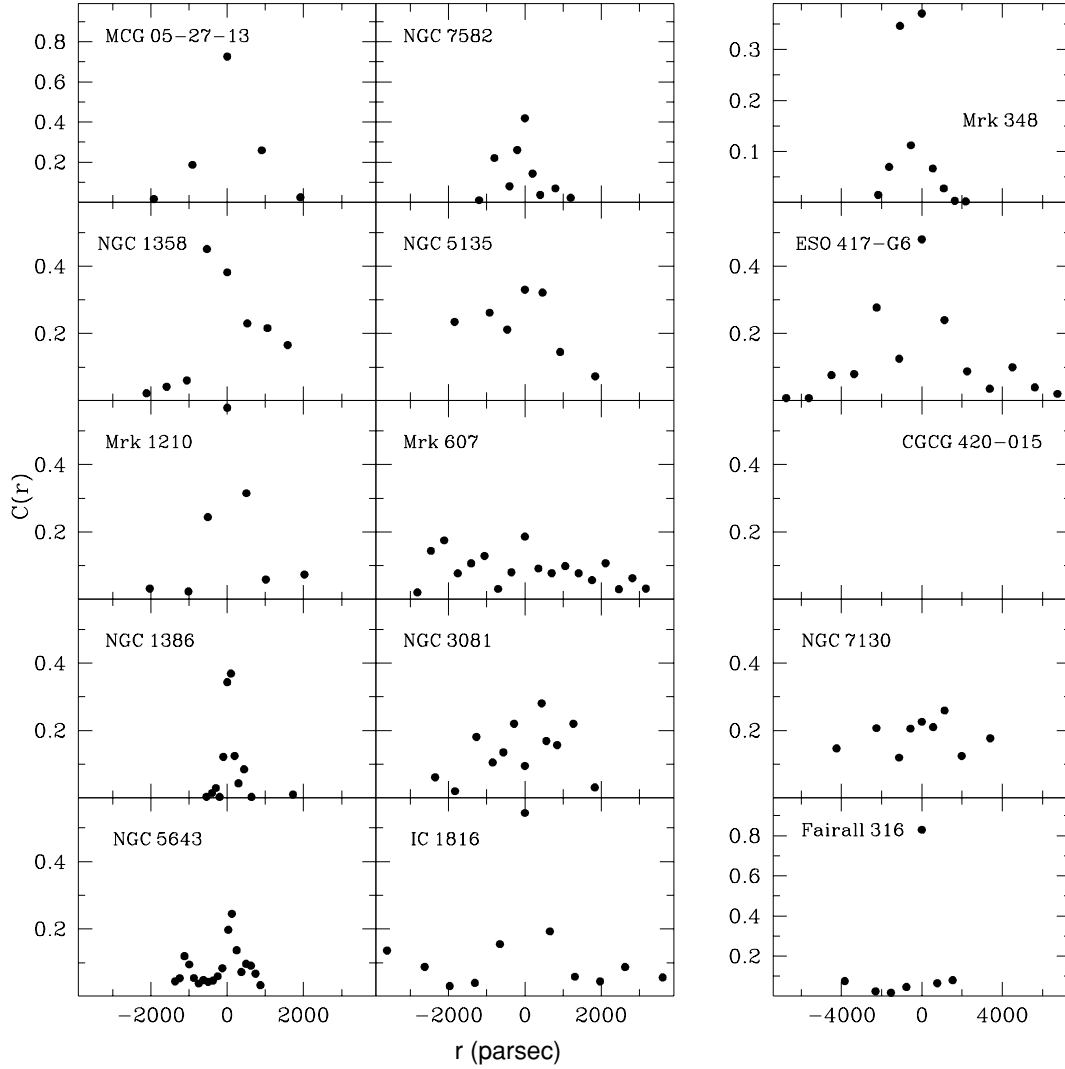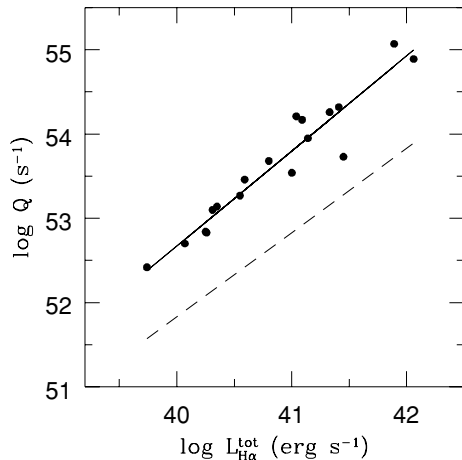
Figure 8. Covering factor distributions.

Figure 9. Q_{sum} (dashed line) and Q_{AGN} (filled circles) versus the total Hα luminosity. The solid line shows a linear regression to the latter relation.

We have repeated the calculations of Q_{AGN} using the derived value of $\alpha_{He\,II}$ instead of the adopted $\alpha = 1.5$ in the previous calculations. This value is also shown in Table 4, together with the corresponding C_{NLR}. The new values of Q_{AGN} and C_{NLR} do not differ much from previous values, confirming that they are not strongly dependent on the value of α, but should be considered more robust because the observations constrain them.

Fig. 10 shows the relation between $\alpha_{He\,II}$ and the highest value of [O III]/Hβ obtained along the NLR+ENLR. This figure shows a trend for the harder continua to be associated with higher values of the [O III]/Hβ ratio.

5 COMPARISON OF THE PREDICTED IONIZING LUMINOSITY WITH OBSERVED HARD X-RAY LUMINOSITIES

In this section we use the derived spectral shape and ionizing luminosity to predict the intrinsic X-ray emission of the galaxy nuclei. In Seyfert 2s, much of this high-energy flux will be absorbed, either by material very close to the nucleus – the torus of the unified model scenario – or other gas in these galaxies, and will therefore not emerge in X-rays. With sufficiently low column densities
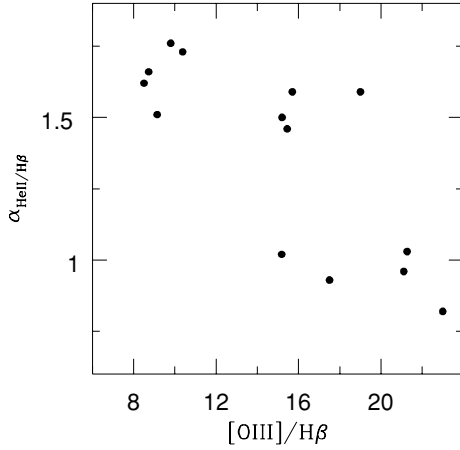
Figure 10. The spectral index $\alpha_{\mathrm{He\,II}}$ versus the [O III]/Hβ ratio.

($N_{\mathrm{H}} < 10^{24}$ cm^{-2}), however, we will detect some of this intrinsic emission directly, particularly at higher energies. In order to predict the intrinsic X-ray luminosity in the 2–10 keV band, $L_{\mathrm{X}}^{\mathrm{pred}}$, we apply the spectral slope $\alpha_{\mathrm{He\,II}}$ appropriate from 13.6 to 54.4 eV that we determined from the He II/Hβ ratio normalized at 13.6 eV by the ionizing luminosity derived from Q_{AGN}, and then extrapolate this SED to X-ray energies. Such an extrapolation has been previously successfully applied to individual galaxies using detailed photoionization modelling (e.g. Alexander et al. 1999). The values of $L_{\mathrm{X}}^{\mathrm{pred}}$ are listed in Table 5.

We compare the predicted intrinsic luminosities with *ASCA* X-ray observations of our sample. We use the reduced data of Levenson, Weaver & Heckman (2001) for NGC 5135, 7130 and 7582, the reduced spectra from the TARTARUS data base for Mrk 1210, NGC 1386, 5643 and Mrk 348, and the spectra extracted in standard *ASCA* processing for NGC 1358 and 3081. The most important spectral components are the buried intrinsic AGN, which we model as a power law, and the scattered AGN contribution, which we model as a power law of the same spectral index, though absorbed only by the Galactic column density. In each case, we fix the spectral index

to the value of $\alpha_{\mathrm{He\,II}}$ measured above. Some cases require Fe Kα fluorescence lines at $E \approx 6.4$ keV. Additional soft components may be present, owing to a thermal starburst or individual sources in the disc of a galaxy, for example. We neglect these in general, however, because we are primarily concerned with higher energies, although we do adopt the more complex best-fitting models of Levenson et al. (2001) in those cases.

We fit these models to the data to determine the observed X-ray luminosity, $L_{\mathrm{X}}^{\mathrm{obs}}$, and the column density to the AGN, $N_{\mathrm{H}}^{\mathrm{X}}$, which are listed in Table 5. We correct for this measured obscuration to obtain the absorption-corrected X-ray luminosity, $L_{\mathrm{X}}^{\mathrm{ac}}$, to estimate the intrinsic luminosity of the buried AGN. For the galaxies with $N_{\mathrm{H}} < 10^{24}$ cm^{-2}, the correction to the measured absorption recovers the intrinsic X-ray emission well because the AGN is directly detected at high energies. In these cases, we find that the spectral extrapolation from the optical and ultraviolet (UV) regime provides a good estimate of the high-energy emission of the AGN.

In the Compton-thick galaxies, which have $N_{\mathrm{H}} > 10^{24}$ cm^{-2}, the buried AGN is not directly measured within the *ASCA* bandpass. In these cases, all the observed 2–10 keV luminosity is caused by the scattered component or additional sources within each galaxy and is not directly related to the total output of the central engine. Single power-law spectral models characterize these examples, typically with the measured $N_{\mathrm{H}} = N_{\mathrm{H}}^{\mathrm{G}}$ (the H I column density from our galaxy), which further implies that we detect only the scattered continuum component. Thus, we expect that $L_{\mathrm{X}}^{\mathrm{ac}}$ severely underpredicts the true X-ray flux. Indeed, we find $L_{\mathrm{X}}^{\mathrm{ac}} \ L_{\mathrm{X}}^{\mathrm{pred}}$ in these cases and suggest that $L_{\mathrm{X}}^{\mathrm{pred}}$ provides an estimate of the intrinsic X-ray emission in Compton-thick galaxies.

We also use $L_{\mathrm{X}}^{\mathrm{pred}}$ to derive the column density from an observed X-ray luminosity, even if an X-ray spectrum is not available. In terms of σ_{E}, the photoelectric cross-section of Morrison & McCammon (1983),
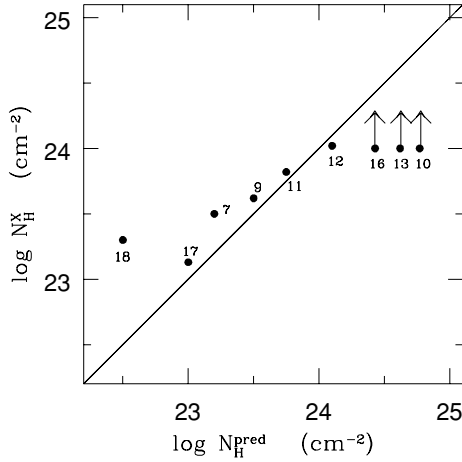
$$L_{\mathrm{X}}^{\mathrm{obs}} = L_{\mathrm{X}}^{\mathrm{pred}} e^{-N_{\mathrm{H}}^{\mathrm{pred}} \sigma_{\mathrm{e}}}. \quad (14)$$

Integrating over the expected power-law SED we obtain the $N_{\mathrm{H}}^{\mathrm{pred}}$ values shown in Table 5, corrected for the Galactic column density. We compare $N_{\mathrm{H}}^{\mathrm{pred}}$ with the values obtained through X-ray

Table 5. H I column densities N_{H} (all in units of cm^{-2}).

Galaxy	$\log N_{\mathrm{H}}^{\mathrm{Gal}}$ (cm^{-2})	$\log L_{\mathrm{X}}^{\mathrm{obs}}$ (erg s^{-1})	$\log L_{\mathrm{X}}^{\mathrm{ac}}$ (erg s^{-1})	$\log N_{\mathrm{H}}^{\mathrm{X}}$ (cm^{-2})	$\log L_{\mathrm{X}}^{\mathrm{pred}}$ (erg s^{-1})	$\log N_{\mathrm{H}}^{\mathrm{pred}}$ (cm^{-2})
ESO 417-G6	20.3	–	–	–	41.59	–
Fairall 316	21.1	–	–	–	41.61	–
CGCG 420-015	20.9	–	–	–	42.21	–
IC 1816	20.4	–	–	–	42.60	–
IRAS 11215−2806	20.8	–	–	–	43.21	–
MCG -05-27-13	20.2	–	–	–	43.45	–
Mrk 1210	20.6	41.77	42.40	23.5	42.23	23.2
Mrk 607	20.7	–	–	–	43.96	–
NGC 1358	20.7	41.54	42.17	23.6	42.18	23.5
NGC 1386	20.1	39.39	39.39	>24	42.74	24.7
NGC 3081	20.7	41.79	42.57	23.8	42.53	23.8
NGC 5135	20.7	41.28	42.41	24.0	42.71	24.1
NGC 5643	20.9	39.87^a	39.87^a	>24	42.58	24.6
NGC 6300	21.0	–	–	–	41.33	–
NGC 6890	20.8	–	–	–	42.47	–
NGC 7130	20.4	40.75	40.78	>24	43.19	24.5
NGC 7582	20.3	41.83	42.25	23.1	42.18	23.0
Mrk 348	20.8	42.26	42.80	23.3	42.38	22.4

^{a}Excluding the Fe Kα line.

Figure 11. Comparison between N_H^X and N_H^{pred}. See Table 1 for galaxy identifications.

spectroscopy in Fig. 11. While this method yields reasonable values of N_H in the Compton-thin cases, it does not accurately measure $N_H > 10^{24}$ cm^{-2}, although it does correctly identify them as being Compton-thick. Fundamentally, equation (14) is inapplicable to the latter because the origin of the detected X-rays, even at energies up to 10 keV, is not the obscured AGN.

With these results, we are confident that the X-ray luminosities predicted from the optical and UV ionizing continuum are reliable estimates of the intrinsic X-ray luminosity. If X-ray fluxes are measured, these can be compared to determine the absorbing column density reasonably well for $N_H < 10^{24}$ cm^{-2}, or correctly identify the Compton-thick cases.

Finally, we compare the neutral column densities along the line of sight to the AGN with the ionized column densities along the ENLR obtained in Section 4.1. The latter range from $10^{20.0}$ to $10^{21.9}$ cm^{-2}, values that are typical of the ionized column densities measured in Seyfert 1 galaxies (Reynolds 1997; George et al. 1998), but two orders of magnitude smaller than the neutral column densities in our sample of Seyfert 2s. Even accounting for the neutral gas contribution in our adopted model of ionization-bounded clouds, the total column density of material along the ENLR is still $<10^{22}$ cm^{-2}. Thus, when the central engines are viewed along the ENLR line of sight, nearly all the hard X-rays emerge unobscured, consistent with what is observed in Seyfert 1 galaxies.

Medium-to-high luminosity AGNs present a big blue bump in the spectral range $14.5 \leqslant \log \nu(\text{Hz}) \leqslant 16.5$ (Elvis et al. 1994). It is difficult to conclude whether or not the big blue bump is present in our sample of galaxies. However, our success in predicting the hard X-ray luminosities using the extrapolated ionizing UV SED may suggest that the SED of our sample are different from the average one of radio-quiet quasars from Elvis et al. (1994, their fig. 10). On the other hand, we have noticed that if we use the average $\alpha_{\text{He II}} = 1.3$ in the radio-quiet high-luminosity AGN SED from Elvis et al. to extrapolate the near-UV SED (at $\sim$912 Å) to the hard X-rays domain we still approximately recover its 4-keV luminosity (within $\approx$30 per cent).

6 COMPARISON BETWEEN THE PREDICTED INFRARED LUMINOSITY AND OBSERVED *IRAS* LUMINOSITY

Another spectral range for which observations of the central luminosity are available – although reprocessed – is the infrared (IR)

IRAS domain. Under the assumption that most of the optical and ultraviolet radiation is absorbed by a dusty torus surrounding the nuclear source, the dust grains near the nucleus will reradiate this energy in the IR. Following the approach of Storchi-Bergmann, Mulchaey & Wilson (1992b), we now compare the observed infrared luminosities with the predicted ones, as follows.

Assuming that the ionizing source is an isotropic radiator and that a dusty torus absorbs all photons incident on it in the wavelength range 100 Å–1 μm, the predicted IR luminosity L_{IR}^{pred} for the torus is given by

$$L_{IR}^{pred} = L_{IR}^{PL} = (1 - C_{cone})Q_{AGN}h\frac{\alpha\nu_0^\alpha}{(1-\alpha)}\left(\nu_2^{1-\alpha} - \nu_1^{1-\alpha}\right), \quad (15)$$

where $C_{cone} = 1 - \cos(\theta)$ is the covering factor of the bicone of escaping radiation with $\theta = 30°$ (see Section 4), h is the Planck constant, $\nu_0 = 3.29 \times 10^{15}$ Hz ($\lambda = 912$ Å), $\nu_1 = 3 \times 10^{14}$ Hz ($\lambda = 1$ μm), $\nu_2 = 3 \times 10^{16}$ Hz ($\lambda = 100$ Å) and $\alpha_{\text{He II}}$ is the slope of the SED derived in Section 4.4 (listed in Table 4).

The above approach assumes that the non-ionizing SED is an extrapolation of the ionizing one. However, this may not be the case, as the SED is not readily observable in Seyfert 2 galaxies. We have thus repeated the above calculation for a non-ionizing part of the SED as given by the average one of Elvis et al. (1994) for radio-quiet quasars, which we have approximated by three segments (hereafter Elvis SED): the first from ν_2 to $\nu_3 = 2.5 \times 10^{15}$ Hz; the second from ν_3 to $\nu_4 = 8.57 \times 10^{14}$ Hz and the third from ν_4 to ν_1. In this case,

$$L_{IR}^{pred} = L_{IR}^{Elvis} = (1 - C_{cone})Q_{AGN}h(s1 + s2 + s3), \quad (16)$$

where

$$s1 = \frac{\alpha\nu_0^\alpha}{(1-\alpha_{\text{He II}})}\left(\nu_2^{1-\alpha_{\text{He II}}} - \nu_3^{1-\alpha_{\text{He II}}}\right) \quad (17)$$

$$s2 = \left(\frac{\nu_3}{\nu_0}\right)^{-\alpha_{\text{He II}}}\nu_3\ln(\nu_3/\nu_4) \quad (18)$$

$$s3 = \frac{\nu_4^{\alpha_{IR}}}{1-\alpha_{IR}}\left(\nu_4^{1-\alpha_{IR}} - \nu_1^{1-\alpha_{IR}}\right) \quad (19)$$

and $\alpha_{IR} = 0.7$.

The results for L_{IR}^{PL} and L_{IR}^{Elvis} are listed in Table 6. The values for L_{IR}^{PL} are larger than those for L_{IR}^{Elvis} ($1.1 < L_{IR}^{PL}/L_{IR}^{Elvis} < 2.7$), as the power-law adopted in the first case predicts larger non-ionizing fluxes than the Elvis SED.

IRAS fluxes are available for 14 galaxies of our sample, which we obtained from the NASA-IPAC Extragalactic Data base (NED). We have calculated the integrated *IRAS* fluxes for each *IRAS* band as in Rowan-Robinson & Crawford (1989). Using the 12- and 25-μm fluxes we have calculated the warm *IRAS* luminosity, L_{IR}^{warm}, and also using the 60- and 100-μm fluxes, the total *IRAS* luminosity, L_{IR}^{tot}, which are listed in Table 6. We show in Fig. 12 a comparison of L_{IR}^{pred} with L_{IR}^{tot}, where open symbols correspond to the power-law SED while filled symbols correspond to Elvis SED. This figure shows that the predicted luminosities are consistent with the observed ones, supporting the adopted simple reradiation model. However, following the discussion of Storchi-Bergmann et al. (1992), we expect that the observed luminosity should be equal to or larger than the predicted luminosity for the torus (because of the large *IRAS* beam, extranuclear sources, such as star-forming regions, may contribute to the *IRAS* fluxes). A closer look at Fig. 12 shows that L_{IR}^{PL} in fact overpredicts the infrared luminosity for the higher-luminosity objects, and in light of the above discussion, the Elvis SED gives a better prediction for the infrared luminosity.
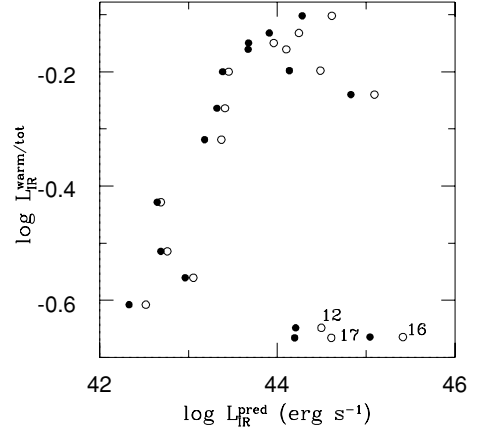
Table 6. IR properties.

Galaxy	log $L_{\rm IR}^{\rm warm}$ (erg s^{-1})	log $L_{\rm IR}^{\rm tot}$ (erg s^{-1})	log $L_{\rm IR}^{\rm PL}$ (erg s^{-1})	log $L_{\rm IR}^{\rm Elvis}$ (erg s^{-1})
ESO 417-G6	43.06	43.22	44.10	43.67
Fairall 316			42.80	42.61
CGCG 420-015	44.00	44.15	43.96	43.67
IC 1816	44.09	44.19	44.61	44.28
IRAS 11215−2806	43.14	43.34	43.45	43.38
MCG -05-27-13	44.53	44.77	45.09	44.83
Mrk 1210	43.75	43.88	44.24	43.91
Mrk 607	43.19	43.46	43.41	43.32
NGC 1358	42.77	43.09	43.37	43.18
NGC 1386	42.21	42.64	42.69	42.65
NGC 3081			43.05	42.98
NGC 5135	43.84	44.49	44.50	44.21
NGC 5643	42.91	43.47	43.06	42.96
NGC 6300	42.80	43.41	42.52	42.33
NGC 6890	43.01	43.53	42.76	42.69
NGC 7130	43.97	44.64	45.41	45.04
NGC 7582	43.45	44.11	44.61	44.19
Mrk 348	43.60	43.80	44.48	44.14

Figure 13. $L_{\rm IR}^{\rm warm}/L_{\rm IR}^{\rm tot}$ versus $L_{\rm IR}^{\rm pred}$ (see the Table 1 for galaxy identifications). Symbols as in Fig. 12.

burst in the *IRAS* domain, which is $L_{\rm IR}^{\rm AGN}/L_{\rm IR}^{\rm SB} \approx 0.5$ for the three cases above.

7 SUMMARY AND CONCLUDING REMARKS

We have used optical long-slit spectroscopy to investigate the properties of the NLR and ENLR of a sample of 18 nearby Seyfert 2 galaxies and to obtain the luminosities of the central sources. The properties of the ENLR were measured within extraction windows corresponding to linear extents at the galaxies in the range 48–570 pc. The NLR is usually included in the nuclear extraction.

Extended emission was observed up to typically 2 kpc from the nucleus, and in a few cases up to 4 kpc. The reddening distribution shows, for approximately half the galaxies for which it could be obtained, smaller values for the NLR than for neighbouring locations of the ENLR. This result could be caused by destruction of the dust by the AGN radiation or optical depth effects, such that only the less obscured regions are observed (Veilleux et al. 1995). The average density of the NLR is $\approx$400 cm^{-3}, and decreases along the ENLR where it reaches the low-density limit.

The [O III] line emission distribution is, on average, more centrally peaked than those of [O II] and Hα. This is caused by a higher excitation closer to the nucleus and decreasing outwards and/or to the contribution of other lower ionization sources (e.g. H II regions) in the outer regions to the [O II] and Hα line emission. The total masses of ionized gas are in the range 10^4–10^7 M$_\odot$.

We have used the Balmer emission-line luminosities of both the NLR and ENLR to derive the rate of ionizing photons radiated by the central source. We have taken into account the geometrical dilution of the nuclear source radiation and assumed that the gas in each extraction window is ionization-bounded. The values obtained for the total number of ionizing photons vary from $10^{52.5}$ to 10^{55} photon s^{-1}, and are, on average, one order of magnitude larger than those that would be obtained merely by integrating the total observed Balmer emission-line luminosities as performed in previous works. The total rate of ionizing photons $Q_{\rm AGN}$ scales with the total (NLR+ENLR) Hα luminosity, which can be used as a calibrator for obtaining $Q_{\rm AGN}$. We find that the average value for the covering factor of the gas in each window along the ENLR is $\sim$0.1.

The spectral slope between 13.6 and 54.4 eV – measured using the He II/Hβ ratio – was used to extrapolate the SED (adopting a power law) from the ionizing UV to hard X-ray domain and to calculate the

Figure 12. $L_{\rm IR}^{\rm tot}$ versus $L_{\rm IR}^{\rm pred}$. Open symbols correspond to $L_{\rm IR}^{\rm pred} = L_{\rm IR}^{\rm PL}$ and filled symbols to $L_{\rm IR}^{\rm pred} = L_{\rm IR}^{\rm Elvis}$.

$L_{\rm IR}^{\rm warm}$ also increases with $L_{\rm IR}^{\rm pred}$. If the IR luminosity is dominated by reprocessed radiation from the torus, this is exactly what we expect. In Fig. 13 we plot the dependence of the ratio $L_{\rm IR}^{\rm warm}/L_{\rm IR}^{\rm tot}$ on $L_{\rm IR}^{\rm pred}$ (where open symbols correspond to the power-law SED while filled symbols correspond to the Elvis SED). This shows that, for most galaxies, $L_{\rm IR}^{\rm warm}/L_{\rm IR}^{\rm tot}$ increases with $L_{\rm IR}^{\rm pred}$, indicating that $L_{\rm IR}^{\rm warm}$ is dominated by reprocessed nuclear radiation. The three galaxies that do not follow the above behaviour are NGC 5135, 7130 and 7582, which have a small $L_{\rm IR}^{\rm warm}/L_{\rm IR}^{\rm tot}$ for their $L_{\rm IR}^{\rm pred}$. These galaxies have composite Seyfert 2 + starburst nuclei, as discussed in previous sections, thus their behaviour can be understood as arising from the large contribution of the circumnuclear starburst, which increases the 60- and 100-µm luminosities and decreases $L_{\rm IR}^{\rm warm}/L_{\rm IR}^{\rm tot}$. If we assume that the AGN in these galaxies follows the same relation between $L_{\rm IR}^{\rm warm}/L_{\rm IR}^{\rm tot}$ and $L_{\rm IR}^{\rm pred}$ as the other galaxies without a circumnuclear starburst, then $\log(L_{\rm IR}^{\rm warm}/L_{\rm IR}^{\rm tot}) \approx -0.2$ for the AGN. We can then derive the relative contribution of the AGN and star-

X-ray luminosity between 2 and 10 keV. Comparing this predicted luminosity with that derived from X-ray data, we conclude that it provides a good estimate of the high-energy emission of the AGN. If the X-ray fluxes are measured, they can be used to determine the N_H columns reasonably well for $N_H < 10^{24}$ cm^{-2} or correctly identify the Compton-thick cases. This result may suggest that most galaxies of our sample do not present the big blue bump observed in high-luminosity AGNs (Elvis et al. 1994), as the ionizing UV SED can be extrapolated to the X-ray domain.

We also compare the *IRAS* observed luminosities with those predicted for an obscuring dusty torus that absorbs all photons with 100 Å $\leqslant \lambda \leqslant 1$ μm incident on it and reradiates in the infrared, using two SEDs: a power-law extrapolated from the UV and that from Elvis et al. (1994). We find that the power-law SED overpredicts the IR fluxes while the Elvis et al. SED gives IR fluxes in better agreement with the *IRAS* values and the reprocessing scenario. In addition we find that the ratio between the warm to total infrared luminosities increases with the predicted luminosity in most cases, indicating that the observed *IRAS* luminosity is dominated by reprocessed nuclear radiation.

ACKNOWLEDGMENTS

REFERENCES

Alexander T., Sturm E., Lutz D., Sternberg A., Netzer H., Genzel R., 1999, ApJ, 512, 204

Antonucci R., 1993, ARA&A, 31, 473

Binette L., Wilson A.S., Storchi-Bergmann T., 1996, A&A, 312, 365

Cid Fernandes R., Storchi-Bergmann T., Schmitt H.R., 1998, MNRAS, 297, 579

Crenshaw D.M., Kraemer S.B., 2000, ApJ, 532, L101

Crenshaw D.M. et al., 2000, AJ, 120, 1731

Elvis M. et al., 1994, ApJS, 95, 1

Evans I., Koratkar A., Allen M., Dopita M., Tsvetanov Z., 1999, ApJ, 521, 531

Fraquelli H.A., Storchi-Bergmann T., Binette L., 2000, ApJ, 532, 867 (FSSB)

George I.M., Turner T.J., Netzer H., Nandra K., Mushotzky R.F., Yaqoob T., 1998, ApJS, 114, 73

González-Delgado R.M., Heckman T., Leitherer C., 2001, ApJ, 546, 845

Kinney A.L., Antonucci R.R.J., Ward M.J., Wilson A.S., Whittle M., 1991, ApJ, 377, 100

Leitherer C., Heckman T.M., 1995, ApJS, 96, 9

Levenson N.A., Weaver K.A., Heckman T.M., 2001, ApJS, 133, 269

Martini P., Pogge R.W., 1999, AJ, 118, 2646

Morrison R., McCammon D., 1983, ApJ, 270, 119

Morse J.A., Raymond J.C., Wilson A.S., 1996, PASP, 108, 426

Mulchaey J.S., Wilson A.S., Tsvetanov Z., 1996a, ApJS, 102, 309

Mulchaey J.S., Wilson A.S., Tsvetanov Z., 1996b, ApJ, 467, 197

Nazarova L.S., O'Brien P.T., Ward M.J., 1997, A&A, 321, 397

Osterbrock D.E., 1989, Astrophysics of Gaseous Nebulae and Active Galactic Nuclei. Univ. Science Books, Mill Valley

Peterson B.M., 1997, An Introduction to Active Galactic Nuclei. Cambridge Univ. Press, Cambridge

Reynolds C.S., 1997, MNRAS, 286, 513

Rowan-Robinson M., Crawford J., 1989, MNRAS, 238, 523

Ruiz J.R., Crenshaw D.M., Kraemer S.B., Bower G.A., Gull T.R., Hutchings J.B., Kaiser M.E., Weistrop D., 2001, AJ, 122, 2961

Schmitt H.R., Kinney A.L., Calzetti D., Storchi-Bergmann T., 1997, AJ, 114, 592

Seaton M.J., 1979, MNRAS, 187, 73P

Storchi-Bergmann T., Wilson A.S., Baldwin J.A., 1992, ApJ, 396, 45

Storchi-Bergmann T., Raimann D., Bica E., Fraquelli H.A., 2000, ApJ, 544, 747

Unger S.W., Pedlar A., Axon D.J., Whittle M., Meurs E.J.A., Ward M.J., 1987, MNRAS, 228, 671

Veilleux S., Kim D.-C., Sanders D.B., Mazzarella J.M., Soifer B.T., 1995, ApJS, 98, 171

Veron-Cetty M.P., Veron P., 2000, Catalog of Quasars and Active Galactic Nuclei, 9th edn, ESO Scientific Report 19, 1

Wilson A.S., Braatz J.A., Heckman T.M., Krolik J.H., Miley G.K., 1993, ApJ, 419, L61

This paper has been typeset from a TeX/LaTeX file prepared by the author.